A Novel Methodology to Automatically Include General Track Flexibility in Railway Vehicle Dynamic Analyses

J. N. Costa[1], P. Antunes[1,2], H. Magalhães[1,2], J. Pombo[1,2,3], J. Ambrósio[1]

[1] LAETA, IDMEC, Instituto Superior Técnico, Universidade de Lisboa, Portugal
[joao.n.costa, jorge.ambrosio]@tecnico.ulisboa.pt

[2] Institute of Railway Research, School of Computing and Engineering, University of Huddersfield, UK
[p.antunes, h.magalhaes, j.pombo]@hud.ac.uk

[3] Instituto Superior de Engenharia de Lisboa, Instituto Politécnico de Lisboa, Portugal

ABSTRACT

The interaction between the rolling stock and the infrastructure plays a crucial role in railway vehicle dynamics. The standard approach consists of using a multibody formulation to model the railway vehicles running on simplified tracks. The track model can be rigid, if it comprises only a geometric description of the rail; semi-rigid, if it considers an elastic foundation underneath the rail; or a moving track model, if it comprises a track section underneath each wheelset traveling with the same speed of the vehicle. Despite their computational inexpensiveness, these approaches do not provide a

complete representation of track flexibility and disregard coupling effects with the vehicle and among the track components. This work proposes a methodology to automatically generate finite element models of railway tracks comprising its relevant flexible components, i.e., rails, pads, fastening systems, sleepers, and ballast or slab. The finite element mesh is generated based on a parametric description of the track that allows an accurate description of its geometry, including curvature, cross-level, grade, and irregularities. The methodology is demonstrated with a case study in which a track with a complex geometry is loaded with two different approaches. The first approach prescribes moving loads, which is a typical approach used to design or analyze the infrastructure. The second approach applies loads retrieved from the dynamic analysis of a complete vehicle. The results show the benefits of this method and reveal that prescribed loading underestimates the forces resulting from the vehicle dynamics, which is an important issue on curved sections.

1 INTRODUCTION

The dynamic analysis of a railway system involves a coupling between two subsystems: the vehicle and the track. This coupling, intimately related to the vehicle-track interaction, is handled differently depending on the subsystem being analysed. In general, studies concerning the dynamic behavior of the railway vehicle model the vehicle using a multibody approach [1–5]. This approach allows predicting, over time, the motion

and forces of the system as a function of its initial conditions and external forces. A multibody system comprises a set of rigid and flexible components interconnected by joints and force elements [6–8]. The joints can be modeled either by perfect kinematic constraints [1,9] or imperfect joints, such as bushings and clearances [10–12]. The force elements are organized into passive elements, such as springs and dampers, or active elements such as actuators [13,14]. The vehicle-track interaction is described with contact models between the wheels and the rails that take into consideration the rolling contact mechanics, and from which the vertical and lateral components of the wheel-rail contact forces are determined [15–19]. In these studies, track modeling focuses on an accurate representation of the geometry of the track [20,21], while the flexibility can be represented with different levels of complexity [22–24]. The least complex approach is to disregard flexibility and consider the rail a rigid structure [18,23,25]. The moving track model is an approach that represents the track as a discrete cross-section that travels below the wheelsets with the same speed of the vehicle [23,26,27]. Note that in the moving track model, the elements comprising the track are rigid bodies, and its flexibility comes from the springs and dampers connecting the bodies. The vehicle-track coupled dynamics model represents the vehicle as a multibody model together with a discretely supported system of elastic beams that represent track flexibility [28–30]. A flexible multibody system approach addresses track flexibility by modeling the rails as finite elements on an elastic foundation [24,31–33]. Finally, there are other approaches taking advantage of the finite

element method to include flexibility in the dynamic analysis of railway vehicles [23,34–37]. These approaches decrease the expensiveness of the procedure by representing the track components as unidimensional or lumped elements, and employing reduction techniques, such as modal synthesis, or cyclic boundaries.

In contrast to railway vehicle dynamics where the assumption of track flexibility can be relaxed, track flexibility becomes essential in railway track dynamics. The dynamic analysis of a track can be performed using either analytical methods, the discrete element method, the boundary element method, or the finite element method. The finite element method is a popular approach where the rails are modeled as beams, the rail pads as spring-damper elements, the sleepers as either beam or continuum elements, and the ballast and sub-ballast as continuum elements [38–45]. When the focus of the study is the track, it is common to use simpler vehicle models, such as prescribed forces, or assemblages of bodies interconnected by spring-damper elements [38,39,46]. Although railway vehicle dynamics models the vehicle-track interaction three-dimensionally [18,25,28], track dynamics often assume the interaction to be vertical [38,40,41,47,48] and seldom include the lateral interaction between the wheel and rail. The assumption of vertical vehicle-track interaction is only reasonable on straight sections, i.e., sections where the track geometry does not change over its length. However, railway tracks have curves, where the lateral interaction is important.

This work proposes a methodology to generate finite element meshes of railway tracks automatically given their design geometry, i.e., curvature, cross-level, grade, and irregularities. A realistic finite element track of Portuguese railways is used as an application example, and its dynamic behavior is analyzed to assess the difference between two different loading approaches. The first approach is based on the standard EN 1991-2 [49], which uses prescribed moving loads. The second approach uses loads extracted from a multibody simulation that considers both the dynamic behavior of a railway vehicle and the wheel-rail contact mechanics.

The flexible track methodology proposed here opens the possibility to study the vehicle-track interaction in a co-simulation environment together with detailed vehicle models [37] in order to study the long-term behavior of the rail infrastructure. This approach can then be used together with suitable track degradation models [5,50–54] to develop decision support tools to promote the implementation of science-based maintenance strategies for the infrastructure and rolling stock.

2 METHODOLOGY FOR MODELING TRACK FLEXIBILITY

2.1 Railway Track Geometry

The geometry of a railway track is commonly described by three variables: horizontal curvature κ, cross-level h, and grade, as functions of the track arc-length s [55,56], as illustrated in Figure 1. The cross-level, seen in Figure 2, is the height difference

between the two rails, and its purpose is to counteract the centrifugal force that tends to overturn the vehicle while curving; the grade is the vertical profile of the track and represents its ascending or descending slope. Transitions between constant curvature sections are assured by transitions curves, in which curvature and cross-level change linearly, as seen in Figure 1.

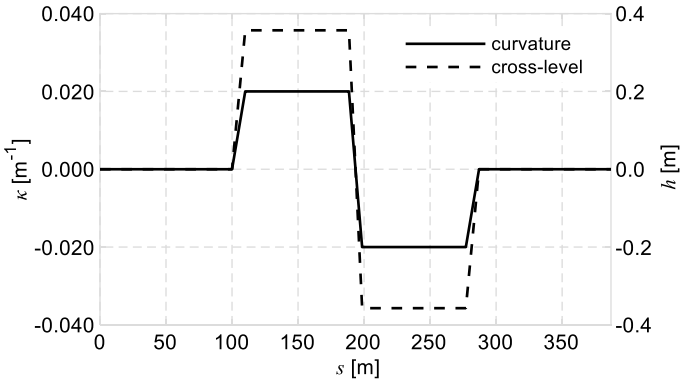

Figure 1: Track curvature and cross-level as a function of the track arc-length.

The parameterization of the track geometry is described as a function of the track arc-length [57]. This parameterization defines the geometry of the track centerline s_c, by discretizing the curvature, cross-level, and grade into a set of points depicted in Table 1. Each point is characterized by a set of coordinates $\mathbf{r}_c = \begin{bmatrix} x & y & z \end{bmatrix}_c^T$, and three orthogonal vectors $(\xi, \eta, \zeta)_c$ that provide an appropriate reference frame based on the cross-level of the track, as observed in Figure 2.

The geometry of the rails is obtained from the geometry of the track centerline. The coordinates of the left and right rail $\mathbf{r}_r$ are obtained using the track gauge, while the reference frames of the rails $(\xi,\eta,\zeta)_r$ are determined from the cross-level of the track and the rail inclination, show in Figure 2. The subscript *r* can be either lr or rr to refer to the left or right rail, respectively. An accurate representation of track geometry requires the left and right rail to be defined separately [17,18,58], especially when the track irregularities are considered [21].

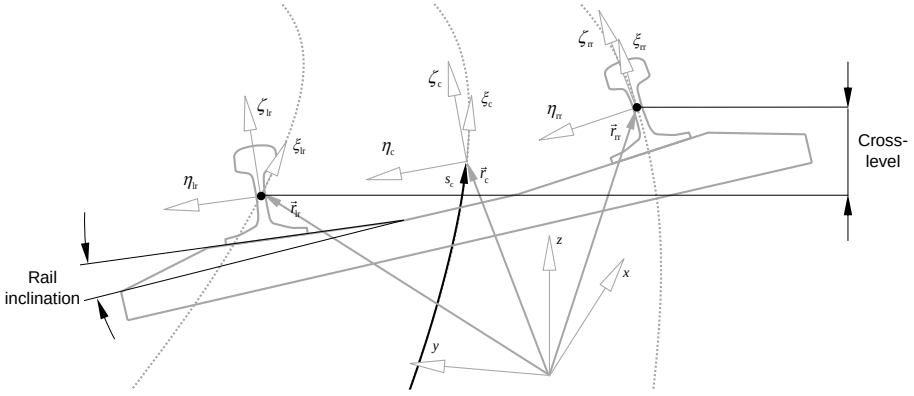

Figure 2: Parametric representation of the track geometry.

Table 1: Parameterization of the design geometry of the track

s_c	$\mathbf{r}_c$	ξ_c	η_c	ζ_c	s_{lr}	$\mathbf{r}_{lr}$	ξ_{lr}	η_{lr}	ζ_{lr}	s_{rr}	$\mathbf{r}_{rr}$	ξ_{rr}	η_{rr}	ζ_{rr}
$s_{c(0)}$	$\mathbf{r}_{c(0)}$	$\xi_{c(0)}$	$\eta_{c(0)}$	$\zeta_{c(0)}$	$s_{lr(0)}$	$\mathbf{r}_{lr(0)}$	$\xi_{lr(0)}$	$\eta_{lr(0)}$	$\zeta_{lr(0)}$	$s_{rr(0)}$	$\mathbf{r}_{rr(0)}$	$\xi_{rr(0)}$	$\eta_{rr(0)}$	$\zeta_{rr(0)}$
…	…	…	…	…	…	…	…	…	…	…	…	…	…	…
$s_{c(n)}$	$\mathbf{r}_{c(n)}$	$\xi_{c(n)}$	$\eta_{c(n)}$	$\zeta_{c(n)}$	$s_{lr(n)}$	$\mathbf{r}_{lr(n)}$	$\xi_{lr(n)}$	$\eta_{lr(n)}$	$\zeta_{lr(n)}$	$s_{rr(n)}$	$\mathbf{r}_{rr(n)}$	$\xi_{rr(n)}$	$\eta_{rr(n)}$	$\zeta_{rr(n)}$

Track irregularities are defined as the difference between the track design configuration and the measurements obtained from the inspection vehicles. The methodology presented here can include cross-level Δh, gauge ΔG, longitudinal level LL_r, and alignment A_r irregularities, as shown in Figure 3 (a). Similar to the track geometry, track irregularities are also defined as functions of the track arc-length and stored in a tabular format.

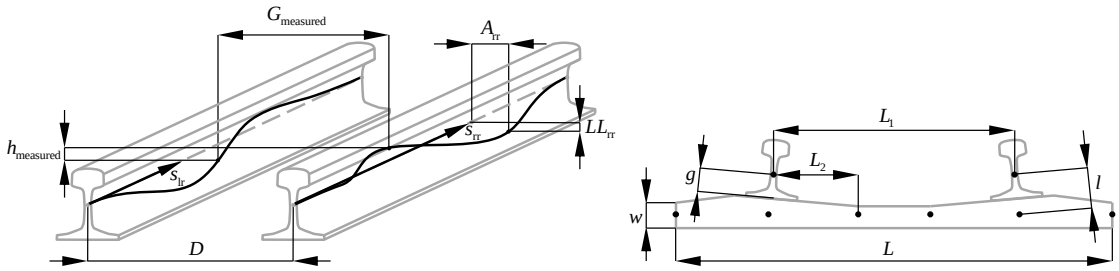

(a) (b)

Figure 3: (a) Parametric representation of the track irregularities, and (b) geometric parameters of the track.

2.2 **Railway Track Structural Components**

The track exhibits a linear dynamic behavior under normal operating conditions. Therefore, the track model is built within the framework of the linear finite element method. The rails and sleepers are modeled using unidimensional elements, based on the Euler-Bernoulli beam theory, with six degrees of freedom per node. Damping plays an important role in the structural dynamics of the track when subjected to the wheel-rail

interaction forces. Proportional damping is assumed here [59,60]. The rail pads are modeled using spring-damper elements connecting the nodes of the elements representing the rails and sleepers, as seen in Figure 4. Finally, the ballast is modeled by two sets of spring-damper elements, below the sleepers and in-between the sleepers.

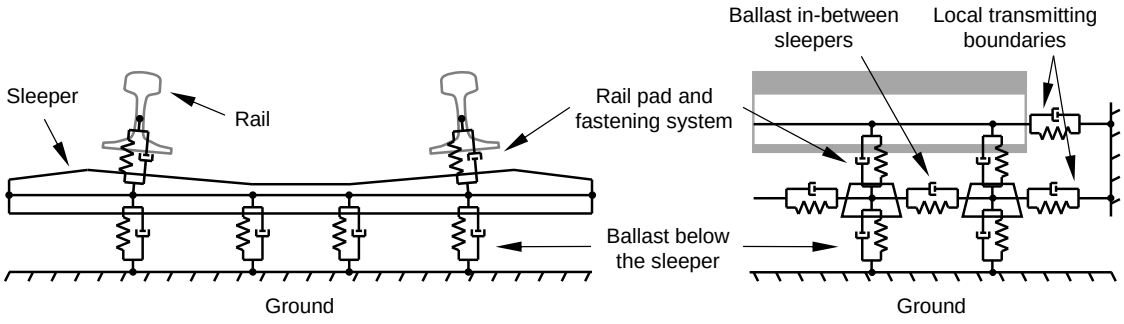

(a) (b)

Figure 4: (a) Cross-section view, and (b) side view of the track model [37].

The division into spring-dampers below and in-between the sleepers is due to the different characteristics of the ballast in these locations. The vertical elements between the sleepers and the ground account for the flexibility of the ballast below the sleepers, as seen in Figure 4, while the horizontal elements in Figure 4 (b) represent the interlocking action of the ballast. The ground represents the sub-ballast and substructure, which are assumed rigid for the purpose of the case study presented in this work.

Local absorbing boundaries, modeled as the spring-damper elements seen in Figure 4 (b), are placed at the ends of the track to attenuate, or eliminate, elastic wave reflection.

Note that spring-damper elements are, in fact, three-dimensional elements. However, in Figures 4 and 5, they are represented as unidimensional for the sake of graphical clarity. The spring-damper element presents translational and torsional characteristics in three perpendicular directions, i.e., each element can be thought of as six spring-dampers overlapped. The rail fastening systems and ballast inertias are modeled by adding lumped masses to the nodes of the finite elements.

2.3 Finite Element Mesh Generation

The generation of the finite element mesh of the railway track requires four sets of inputs: the track design geometry listed in Table 1, the track irregularities, the geometric parameters depicted in Figure 3 (b), and the properties listed in Tables 2 and 3. Note that the geometric and material properties can also be parameterized as a function of the track arc-length to allow for track sections with different properties.

Table 2: Properties of the beam elements in the track model

Element properties	Rail	Ref.	Sleeper	Ref
Young modulus - E [Pa]	2.10×10^{11}	61	3.10×10^{10}	62
Torsion modulus - G [Pa]	8.08×10^{10}		1.50×10^{10}	63
Cross-section area - A [m^2]	7.67×10^{-3}	64	5.6×10^{-2}	62
Torsional constant in $\eta\zeta$ Plane - $J_{\xi\xi}$ [m^4]	2.21×10^{-6}		1.71×10^{-3}	
Second moment of area in $\xi\zeta$ Plane - $I_{\eta\eta}$ [m^4]	3.04×10^{-5}	64	2.60×10^{-4}	
Second moment of area in $\xi\eta$ Plane - $I_{\zeta\zeta}$ [m^4]	5.12×10^{-6}	64	1.67×10^{-4}	
Density ρ [kg/m^3]	7860	65	2750	61
Rayleigh damping parameter - α [s^{-1}]	3.98×10^{-4}		3.98×10^{-4}	
Rayleigh damping parameter - β [s]	0.94		0.94	

Table 3: Properties of the spring-damper elements in the track model

Element properties	Pads	Ref.	Ballast bellow the sleepers	Ref.	Ballast in-between sleepers	Ref.
Vertical stiffness - K_v [N/m]	2.50×10^8	66	6.19×10^7	67	5.50×10^5	68
Lateral stiffness - K_{lat} [N/m]	5.00×10^7	66	1.00×10^7	68	4.05×10^5	68
Longitudinal stiffness - K_l [N/m]	5.00×10^7	66	5.50×10^5		3.92×10^7	65
Vertical torsional stiffness - K_{rv} [Nm/rad]	2.60×10^5	66	-		-	
Lateral torsional stiffness - K_{rlat} [Nm/rad]	8.33×10^5	66	-		-	
Longitudinal torsional stiffness - K_{rl} [Nm/rad]	4.69×10^5	66	-		-	
Vertical damping - C_v [Ns/m]	3.00×10^4	66	2.94×10^4	65	2.94×10^4	
Lateral damping - C_{lat} [Ns/m]	3.00×10^4	66	2.94×10^4		2.94×10^4	
Longitudinal damping - C_l [Ns/m]	3.00×10^4	66	2.94×10^4		2.94×10^4	65
Vertical torsional damping - C_{rv} [Nsm/rad]	1.00×10^2	66	-		-	
Lateral torsional damping - C_{rlat} [Nsm/rad]	1.00×10^2	66	-		-	
Longitudinal torsional damping - C_{rl} [Nsm/rad]	1.00×10^2	66	-		-	
Lumped mass - m [kg]	2.5		226.41	67	-	

Given the track geometry information and the structural properties of the track components, this work proposes a methodology to generate the complete finite element model of the track systematically. Particular attention is given to defining the position of the finite element nodes. The structural elements are defined by three nodes, with nodes *i* and *j* defining the geometry of the element, and node *k* defining its orientation, as depicted in Figure 5 (a).

2.3.1 Rail nodes

The position of the nodes in the finite element mesh defines the structure of the track. For each cross-section, the position of the structural nodes representing the rail finite elements is evaluated as

$$\begin{aligned} \mathbf{r}_1 &= \mathbf{r}_{\mathrm{lr}} \\ \mathbf{r}_2 &= \mathbf{r}_{\mathrm{rr}} \end{aligned} \tag{1}$$

where $\mathbf{r}_{\mathrm{lr}}$ and $\mathbf{r}_{\mathrm{rr}}$, refer the left and right rail coordinates provided in Table 1. The subscripts 1 and 2 refer to the local node numbering of the track cross-section depicted in Figure 5 (b).

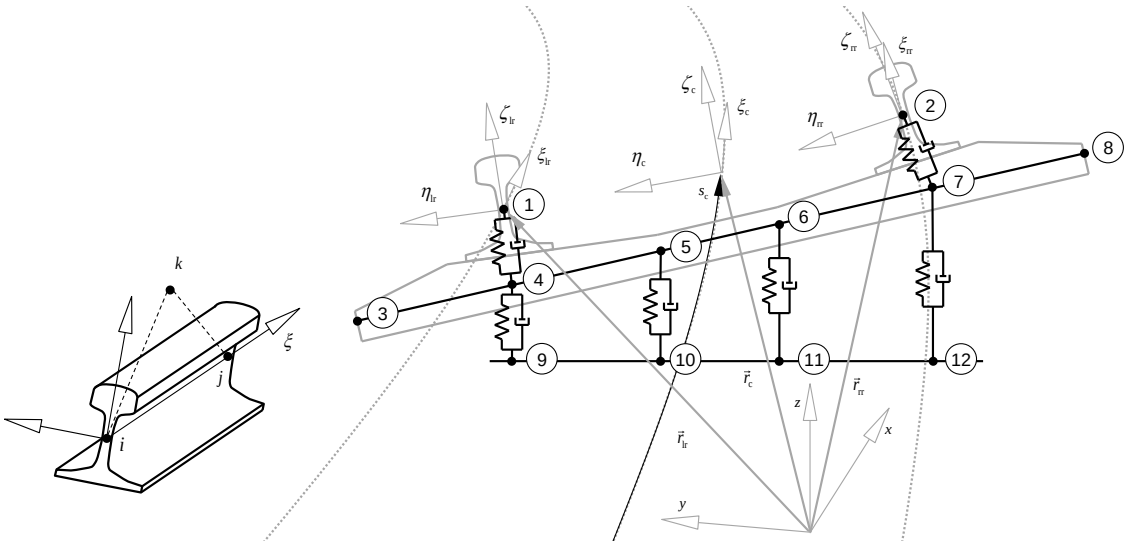

(a) (b)

Figure 5: (a) Finite element with structural nodes *i* and *j*, and orientation node *k*, and (b) cross-section of the track finite element model with local numbering depicted as *i*.

The position of the orientation node associated with a rail finite element is evaluated as

$$\mathbf{r}_{k,r} = \frac{\mathbf{r}_r^{s-1} + \mathbf{r}_r^{s}}{2} + b\left(\frac{\zeta_r^{s-1} + \zeta_r^{s}}{2}\right) \tag{2}$$

where the subscript r can be either lr or rr, to specify the left or right rail, and the superscript s corresponds to the track arc-length. The variable b places the orientation node off-axis and can take any non-null value. Note that rail inclination is ensured by placing the orientation node according to the component ζ of the rail.

2.3.2 Sleeper nodes

The positions of the structural nodes representing a sleeper, as seen in Figure 5 (b), are evaluated as

$$\begin{aligned} \mathbf{r}_3 &= \mathbf{r}_4 + \eta_{\mathrm{c}}\left(\frac{L - L_1}{2}\right) & \mathbf{r}_6 &= \mathbf{r}_7 + \eta_{\mathrm{c}} L_2 \\ \mathbf{r}_4 &= \mathbf{r}_1 - \zeta_{\mathrm{lr}} l & \mathbf{r}_7 &= \mathbf{r}_2 - \zeta_{\mathrm{rr}} l \\ \mathbf{r}_5 &= \mathbf{r}_4 - \eta_{\mathrm{c}} L_2 & \mathbf{r}_8 &= \mathbf{r}_7 - \eta_{\mathrm{c}}\left(\frac{L - L_1}{2}\right) \end{aligned} \tag{3}$$

where the quantities L, L_1, L_2, and l are the sleeper dimensions depicted in Figure 3 (b). The distance l is evaluated using the geometric parameters of the track. Only one orientation node per sleeper is defined because all its elements have the same orientation. The position of the orientation node associated with a sleeper is evaluated as

$$\mathbf{r}_k = \mathbf{r}_{\mathrm{c}} + b\zeta_{\mathrm{c}} \tag{4}$$

2.3.3 Rail Pad Nodes

The positions of the structural nodes representing a rail pad in the cross-section are already defined. The element representing a rail pad is defined by connecting the rail node to the sleeper node, as implied in Figure 5 (b). The position of the orientation node associated with a rail pad element is evaluated as

$$\mathbf{r}_{k,r} = \frac{1}{2}\left(\mathbf{r}_i + \mathbf{r}_j\right) + b\eta_r \tag{5}$$

where the subscript *r* can be either lr or rr, to specify the left or right rail, and subscripts *i* and *j* are 1 and 4 for the left rail, or 2 and 7 for the right rail.

2.3.4 Ballast and Boundary nodes

The elements representing the flexibility of the ballast in-between the sleepers are defined by connecting the structural nodes of consecutive sleepers, as seen in Figure 4 (b). Due to the cross-level of the track, each of these elements needs an orientation node. Their position is evaluated as

$$\mathbf{r}_k = \tfrac{1}{2}\left(\mathbf{r}_n + \mathbf{r}_{n-1}\right)_m + b[0 \quad 0 \quad 1]^T, \quad m = 4,5,6,7 \tag{6}$$

where subscript *n* refers to the sleeper number, and subscript *m* refers to the structural nodes of the sleeper shown in Figure 5 (b).

Boundary nodes are placed directly below the sleeper structural nodes and leveled at a particular height, as shown in Figure 5 (b). The elements representing the flexibility

of the ballast below the sleepers are defined by connecting the boundary nodes to the structural nodes of the sleepers. Since these elements lay in the same plane, only one orientation node per section is necessary. Nodes 5 and 10 are arbitrarily chosen to evaluate the position of the orientation node as

$$\mathbf{r}_k = \tfrac{1}{2}\left(\mathbf{r}_5 + \mathbf{r}_{10}\right) + b\eta_c \tag{7}$$

The positions of the boundary nodes at the ends of the track are defined based on the position of the first and last sleeper as

$$\mathbf{r}_j = \mathbf{r}_i + b\xi_c, \qquad i = 1,2,4,5,6,7 \tag{8}$$

The elements representing the local absorbing boundaries are defined by connecting nodes *i* and *j* in equation (8), and their respective orientation nodes are evaluated as

$$\mathbf{r}_k = \tfrac{1}{2}\left(\mathbf{r}_i + \mathbf{r}_j\right) + b[0 \quad 0 \quad 1]^T, \qquad i = 1,2,4,5,6,7 \tag{9}$$

The track comprises sections where the rails are supported by the sleepers, and sections where the rails are unsupported. Nodes 1 through 12 are generated at track arc-lengths corresponding to multiples of the distance between sleepers. Any other track lengths correspond to unsupported sections, i.e., sections in-between sleepers, and therefore, only nodes 1 and 2 are generated. The boundary nodes are fixed.

The correspondence between the numbering the rail elements and the arc-length of their nodes is stored in a tabular structure. This structure identifies the rail elements that

the wheel-rail forces are applied to while a vehicle is moving. Therefore, the numbering of the finite elements associated with the rails is of fundamental importance for an efficient search of the contact points in the wheel-rail contact. Furthermore, the numbering of the finite element mesh is also important to minimize the bandwidth of the finite element global matrices, thus improving the efficiency of the numerical solution process.

2.3.5 Track Irregularities

Let the finite element, in which wheel-rail contact occurs, connect nodes *i* and *j*. The displacement and rotations of a cross-section of the element are obtained using the finite element beam shape functions as

$$\begin{Bmatrix} \boldsymbol{\delta}_r \\ \boldsymbol{\theta}_r \end{Bmatrix} = \begin{bmatrix} \mathbf{A}_e & \\ & \mathbf{A}_e \end{bmatrix} \begin{bmatrix} \mathbf{N}_i^{dd}(\xi) & \mathbf{N}_i^{d\theta}(\xi) & \mathbf{N}_j^{dd}(\xi) & \mathbf{N}_j^{d\theta}(\xi) \\ \mathbf{N}_i^{\theta d}(\xi) & \mathbf{N}_i^{\theta\theta}(\xi) & \mathbf{N}_j^{\theta d}(\xi) & \mathbf{N}_j^{\theta\theta}(\xi) \end{bmatrix} \begin{bmatrix} \mathbf{A}_e & & & \\ & \mathbf{A}_e & & \\ & & \mathbf{A}_e & \\ & & & \mathbf{A}_e \end{bmatrix}^T \begin{Bmatrix} \boldsymbol{\delta}_i \\ \boldsymbol{\theta}_i \\ \boldsymbol{\delta}_j \\ \boldsymbol{\theta}_j \end{Bmatrix} \tag{10}$$

where $\boldsymbol{\delta}_i$ and $\boldsymbol{\delta}_j$ are the nodal displacements, $\boldsymbol{\theta}_i$ and $\boldsymbol{\theta}_j$ are the nodal rotations, all expressed in the inertial reference frame, $\mathbf{A}_e$ is the element transformation matrix from the local reference frame to the inertial reference frame, and $\mathbf{N}^{dd}$, $\mathbf{N}^{d\theta}$, $\mathbf{N}^{\theta d}$, and $\mathbf{N}^{\theta\theta}$ are sub-matrices with the shape functions of the beam element [69]. Equation (10) is a function of the natural

coordinate of the element in which contact takes place, $\xi = \left(s_r - s_i\right) / \left(s_j - s_i\right)$, where s_r is the arc-length of the rail up to the contact point, and s_i and s_j are the arc-lengths of the rail up to nodes *i* and *j*, respectively. The track irregularities are not included directly into the finite element model of the track. However, they are taken into account in a scenario where the vehicle-track interaction is simulated online, and the contact model allows the vehicle and the track to exchange data.

The position of the rail is updated to include the track displacement and track irregularities as

$$\begin{aligned} \mathbf{r}_r &= \mathbf{r}\left(s_r\right) + \boldsymbol{\delta}_r + \mathbf{A}_{\mathrm{c}} \begin{bmatrix} 1 & 0 & 0 \\ 0 & \cos\Delta\varphi & -\sin\Delta\varphi \\ 0 & \sin\Delta\varphi & \cos\Delta\varphi \end{bmatrix} \boldsymbol{\delta}_r^{\mathrm{irr}} \\ \boldsymbol{\delta}_{\mathrm{lr}}^{\mathrm{irr}} &= \begin{Bmatrix} 0 \\ \dfrac{D}{2} + A_{\mathrm{lr}} + \dfrac{\Delta G}{2} \\ LL_{\mathrm{lr}} \end{Bmatrix}, \quad \boldsymbol{\delta}_{\mathrm{rr}}^{\mathrm{irr}} = \begin{Bmatrix} 0 \\ -\dfrac{D}{2} + A_{\mathrm{rr}} - \dfrac{\Delta G}{2} \\ LL_{\mathrm{rr}} \end{Bmatrix} \end{aligned} \tag{11}$$

where $\mathbf{r}\left(s_r\right)$ is the position of the center of the rail cross-section that includes the contact point, $\boldsymbol{\delta}_r$ is the interpolated displacement of the rail cross-section, $\Delta\varphi = \arcsin\left(\Delta h / D\right)$ represents the roll of the track due to the cross-level irregularity, *D* is the distance between the geometric centers of the rails, as depicted in Figure 3 (a), $\mathbf{A}_c = \begin{bmatrix} \mathbf{u}_\xi & \mathbf{u}_\eta & \mathbf{u}_\zeta \end{bmatrix}_{\mathrm{c}}$ is the transformation matrix from the track reference frame to the inertial reference frame, and

$\boldsymbol{\delta}_r^{\text{irr}}$ is a vector compromising the irregularities expressed in the track reference frame, as described in subsection 2.1. Subscript *r* can be either lr or rr to refer to the left and right rail, respectively.

2.3.6 Example of Railway Track Finite Element Model

Figure 6 shows an example of a railway track mesh generated using the methodology proposed. The track consists of a straight section of 100 m, followed by a quarter-circular left-handed curve, a quarter-circular right-handed curve, and another straight section of 100 m, as depicted in Figure 1. The circular sections have a 50 m radius, and the transition curves are 10 m long. Note that the curvature, cross-level, and length of the transition curves do not respect the limits of the European standards [70]. This example shows that the proposed methodology can model any track geometry given in the format described in subsection 2.1.

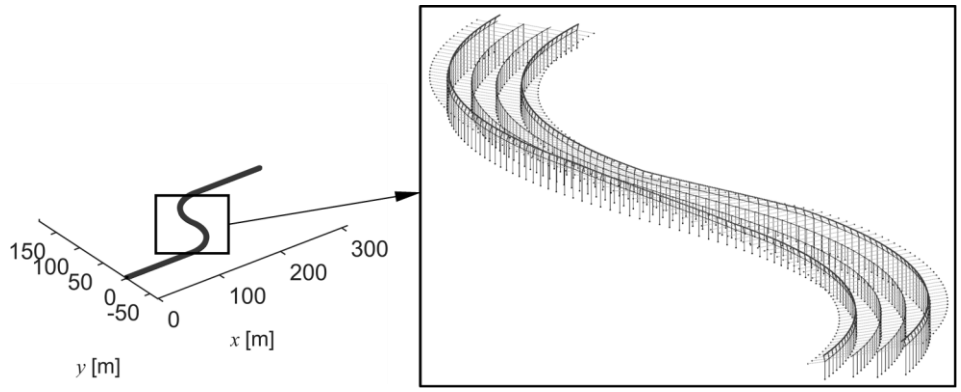

(a) (b)

Figure 6: Railway track with sharp curves generated using the methodology proposed: (a) track mesh, (b) close-up of the change in curvature and cross-level.

3 TRACK LOADING BY RAILWAY VEHICLES

Railway studies focusing on the track tend to simplify the vehicle-track interaction and disregard some aspects of the wheel-rail contact mechanics. This interaction is usually based on the assumption that both the displacement of the wheelset from the central position of the track, and the relative velocities are small. This assumption is reasonable in a straight section but does not capture relevant dynamic phenomena on a curved section. This work considers two different approaches that represent vehicle-track interaction in railway applications dealing with track flexibility. The first approach, referred to as simplified loading in this work, is used for structural applications in civil engineering and assumes that the inertia forces of the vehicle represent the vehicle-track interaction [49]. The second approach, referred to as realistic loading in this work, uses a multibody model of a complete vehicle, and describes the vehicle-track interaction with a three-dimensional wheel-rail contact model. The resulting normal and tangential forces are used to load the track.

3.1 Simplified Track Loading

The simplified track loading approach assumes that the wheel-rail interaction is modeled by the inertia of the vehicle moving at a constant speed. The horizontal wheel-

rail forces are computed using the European standard expression for centrifugal loads on curved bridges [49]

$$f_{\eta'} = \frac{c_1 \kappa v^2}{g} f_{\zeta'} \tag{12}$$

where $f_{\zeta'}$ is the vertical force, κ is the track curvature, v is the speed of the vehicle, c_1 is a reduction factor, g is the gravitational acceleration, and subscripts ζ' and η' refer to the vertical and lateral direction, respectively. The standard provides values for the reduction factor and vertical forces $f_{\zeta'}$ depending on the type of vehicle that operates the track. However, since one of the goals of this work is to discuss the difference between the use of simplified and realistic loading, the reduction factor is ignored, and the vertical forces are computed as

$$f_{\zeta'} = \frac{Mg}{n_w} \tag{13}$$

where M is the mass of the vehicle, g is the gravitational acceleration, and n_w is the number of wheels.

3.2 **Realistic Track Loading**

The realistic track loading approach uses the wheel-rail contact force history obtained from the dynamic analysis of a railway vehicle running on a rigid track. The forces and respective points of application are determined by the wheel-rail contact model

proposed by Pombo *et al.* [17,18,21]. This subsection is a brief description of the strategy, and a detailed description of the methodologies is found in [17,18,21].

The identification of the interference between each wheel-rail pair requires the parameterization of the wheel and rail surfaces. The wheel profile is defined by two sets of nodal points, one for the tread and another for the flange, as depicted in Figure 7 (a). Note that by describing the wheel tread and flange by two sets of nodal points, contact can occur in two different points simultaneously. The nodal points are interpolated to define the cross-section of the wheel profile as a function of the parameter u_w. The cross section is then swept from ξ_w around the wheel axes η_w, by the angle s_w, to form the parametric surface of revolution that defines the geometry of the wheel. The rail profile is also obtained by interpolation of a set of nodal points as a function of u_r, which in turn is swept from the origin of the rail along its arc-length s_r. Figure 7 (b) depicts the parametric surfaces of the wheel and the rail. In both cases, cubic splines are used to obtain smooth surfaces representing the rails, wheel treads, and wheel flanges. This parameterization allows performing a contact search in which, upon identifying effective contact, the position of the contact points and their respective normal and tangent vectors are obtained.

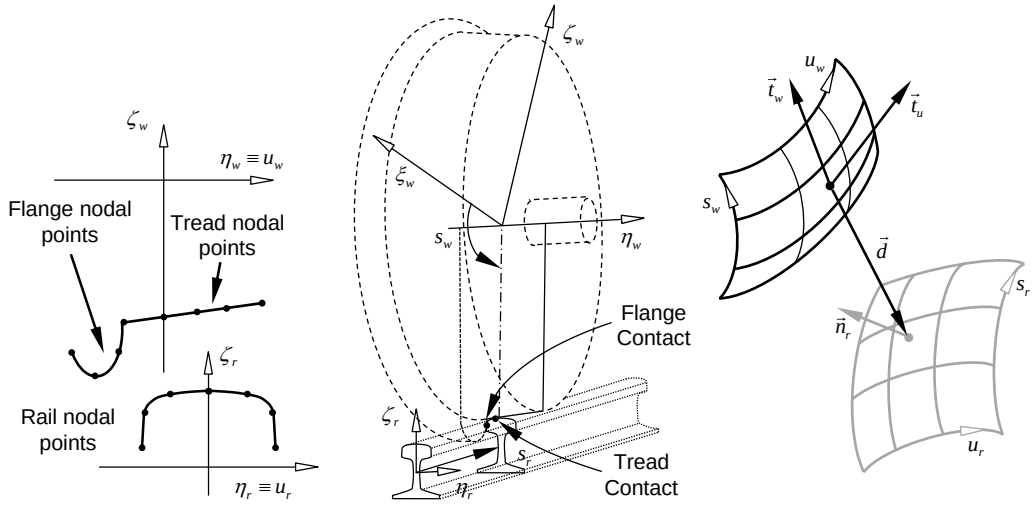

(a) (b) (c)

Figure 7: (a) Profiles of the wheel tread, wheel flange, and rail, their (b) parametric surfaces, and (c) search for candidate points between two contact surfaces [37]

Given the wheel and rail parametric surfaces, the contact detection problem is solved in two steps. In the first step, the candidate contact points are determined by geometric relations between the two surfaces, which are represented by the following nonlinear system of equations [17,18,21]

$$\begin{cases} \mathbf{d}^T \mathbf{t}_u = 0 \\ \mathbf{d}^T \mathbf{t}_w = 0 \\ \mathbf{n}_r^T \mathbf{t}_u = 0 \\ \mathbf{n}_r^T \mathbf{t}_w = 0 \end{cases} \tag{14}$$

where **d** is the vector between the candidate contact points, $\mathbf{n}_r$ is the normal vector, $\mathbf{t}_u$ and $\mathbf{t}_w$ are the tangent vectors, all defined as functions of the surface parameters s_r, u_r, s_w, and u_w, as represented in Figure 7 (c).

The second step is to assess if there is an interference between the surfaces. The interference condition is evaluated as

$$\mathbf{d}^T \mathbf{n}_r > 0 \tag{15}$$

When equation (15) is fulfilled for a particular contact pair, there is contact between the wheel and the rail, and the normal and tangential forces are evaluated. The normal force is evaluated using a Hertzian contact model with hysteresis damping as [71,72]

$$f_{\mathrm{n}} = K\left(1+\frac{3(1-e)}{4}\frac{\dot{\delta}}{\dot{\delta}^{\max}}\right)\delta^{1.5} \tag{16}$$

where K is the stiffness constant related to the geometry and material properties of the surfaces in contact, e is the coefficient of restitution, δ is the amount of interference between the surfaces, $\dot{\delta}$ is the interference velocity, and $\dot{\delta}^{\max}$ is the maximum value of $\dot{\delta}$ during the interference.

The tangential forces are evaluated using the method proposed by Polach [16] in which the longitudinal force is calculated as

$$f_{\xi} = f\frac{\upsilon_{\xi}}{\upsilon_{\mathrm{C}}} \tag{17}$$

and the lateral force is evaluated as

$$f_\eta = f\frac{\upsilon_\eta}{\upsilon_C} + f_{\eta S}\frac{\phi}{\upsilon_C} \tag{18}$$

where f is the tangential contact force caused by longitudinal and lateral relative velocities between the contacting surfaces, generally designated as creepages in rolling contact, υ_ξ, υ_η, and ϕ are the longitudinal, lateral, and spin creepages at the point of contact, υ_C is the modified translational creepage, which accounts for the effect of spin creepage, and $f_{\eta S}$ is the lateral tangential force due to spin creepage.

3.3 **Wheel Loading in the Finite Element Track Model**

The dynamic equilibrium equations of the railway track model are written as [59,73]

$$\mathbf{M}\ddot{\mathbf{u}} + \mathbf{C}\dot{\mathbf{u}} + \mathbf{K}\mathbf{u} = \mathbf{f} \tag{19}$$

where **M**, **C**, and **K** are the finite element global mass, damping, and stiffness matrices, and $\ddot{\mathbf{u}}$, $\dot{\mathbf{u}}$, **u** and **f** are the acceleration, velocity, displacement, and force vectors, respectively. The global matrices **M**, **C**, and **K** are built by assembling the individual finite element matrices according to the topology of the track mesh. The force vector **f** is evaluated during the time integration, at every time step, and represents the equivalent wheel-rail contact forces and moments. The force vector is computed from a time history

of the wheel-rail forces and contact parameters retrieved from the dynamic analysis of the railway vehicle.

In the wheel-rail contact model described, the contact forces are applied on the surface of the rail. However, the beam element used to describe the rails only models their geometric center. Furthermore, the wheel-rail forces move along the rails, but the finite element method requires that the lumped forces are applied to the nodes of the elements. Therefore, an equivalent force $\mathbf{f}_e$, and a transport moment $\mathbf{n}_e$, are evaluated using the contact forces and applied to the geometric center of the rail as depicted in Figure 8 (a). This equivalent force system is then transferred to the nodes of the finite element beam representing the rails, as observed in Figure 8 (c) and (d).

The equivalent force system at the geometric center of the beam is given by

$$\begin{aligned} \mathbf{f}_e &= \mathbf{f}_{\text{tr}} + \mathbf{f}_{\text{fl}} \\ \mathbf{n}_e &= \tilde{\mathbf{s}}_{\text{tr}}\mathbf{f}_{\text{tr}} + \tilde{\mathbf{s}}_{\text{fl}}\mathbf{f}_{\text{fl}} \end{aligned} \tag{20}$$

where $\mathbf{s}_{\text{tr}}$ and $\mathbf{s}_{\text{fl}}$ are the contact position vectors with respect to the cross-section center defined in the inertial reference frame. The transformation of the contact position points from the rail cross-section to the inertial reference frame is obtained by $\mathbf{s}_{\text{tr}} = \mathbf{A}_r\mathbf{s}'_{\text{tr}}$ and $\mathbf{s}_{\text{fl}} = \mathbf{A}_r\mathbf{s}'_{\text{fl}}$ with the transformation matrix $\mathbf{A}_r = \begin{bmatrix} \mathbf{u}_\xi & \mathbf{u}_\eta & \mathbf{u}_\zeta \end{bmatrix}_r$. In this notation, $\tilde{\mathbf{v}}$ is used to represent the cross product as matrix multiplication using a skew-symmetric

matrix built with the components of **v**. The equivalent force system is also easily adapted to accommodate the simplified loading by considering

$$\begin{aligned} \mathbf{f}_e &= \mathbf{A}\mathbf{f}_{\text{simplified}} \\ \mathbf{n}_e &= \mathbf{0} \end{aligned} \tag{21}$$

where $\mathbf{A} = \begin{bmatrix} \mathbf{u}_\xi & \tilde{\mathbf{u}}_{\zeta'}\mathbf{u}_\xi & \mathbf{u}_{\zeta'} \end{bmatrix}$ is the transformation matrix from the simplified force reference frame to the inertial reference frame, as seen in Figure 8 (b), and $\mathbf{f}_{\text{simplified}} = \begin{bmatrix} 0 & f_{\eta'} & f_{\zeta'} \end{bmatrix}$ is a force vector built with the forces described in subsection 3.1.

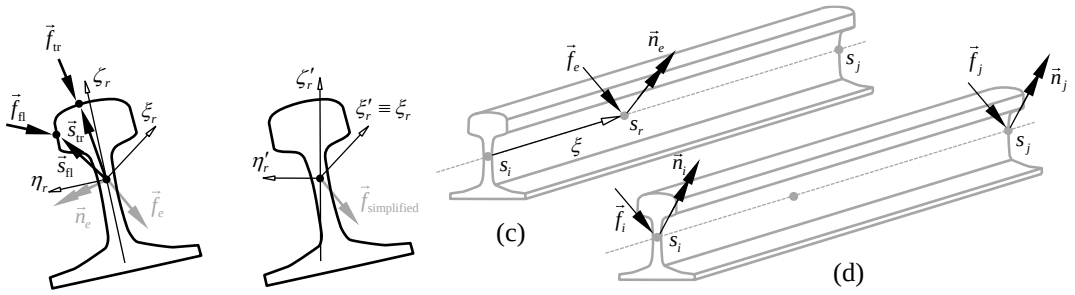

Figure 8: (a) Equivalent force system due to realistic loading, (b) equivalent force system due to simplified loading, (c) wheel-rail contact force along the rail element, and (d) forces on the nodes of the rail finite element.

Finally, the equivalent forces system is transferred to the nodes of the elements representing the rails using the beam shape functions as

$$\begin{Bmatrix} \mathbf{f}_i \\ \mathbf{n}_i \\ \mathbf{f}_j \\ \mathbf{n}_j \end{Bmatrix} = \begin{bmatrix} \mathbf{A}_e & & & \\ & \mathbf{A}_e & & \\ & & \mathbf{A}_e & \\ & & & \mathbf{A}_e \end{bmatrix} \begin{bmatrix} \mathbf{N}_i^{dd}(\xi) & \mathbf{N}_i^{d\theta}(\xi) & \mathbf{N}_j^{dd}(\xi) & \mathbf{N}_j^{d\theta}(\xi) \\ \mathbf{N}_i^{\theta d}(\xi) & \mathbf{N}_i^{\theta\theta}(\xi) & \mathbf{N}_j^{\theta d}(\xi) & \mathbf{N}_j^{\theta\theta}(\xi) \end{bmatrix}^T \begin{bmatrix} \mathbf{A}_e & \\ & \mathbf{A}_e \end{bmatrix}^T \begin{Bmatrix} \mathbf{f}_e \\ \mathbf{n}_e \end{Bmatrix}$$

(22)

where $\mathbf{f}_i$, $\mathbf{f}_j$, $\mathbf{n}_i$, and $\mathbf{n}_j$ are the forces and moments applied to nodes *i* and *j*, and $\mathbf{A}_e$ is the finite element transformation matrix from the local reference frame to the inertial reference frame. The remaining variables were described in equation (10).

The dynamic equilibrium equations of the track are solved using an integration algorithm based on the implicit Newmark trapezoidal rule due to its unconditional stability when used implicitly [59]. However, note that the methodology described here is independent of the algorithm chosen for time integration.

4 RESULTS

4.1 Case Study – Suburban Track Line

A case study demonstrates the methodologies described in this work. A finite element model of a Portuguese railway track is generated and its dynamic behavior is analyzed using the two alternative loading approaches described in section 3. The track comprises a straight section, followed by a right-hand curve, a straight section, a left-

handed curve, and another straight section, as seen in Figure 9. The track has an Iberian gauge with UIC60 rail profiles and a 1/20 inclination. Tables 2 and 3 compile the properties used for the finite element track model. For both loading approaches, i.e., the simplified and realistic loading, the vehicle moves at a constant speed of 60 km/h, which is the maximum allowed speed for this track. The realistic loading of the railway track is obtained by performing a dynamic analysis of a passenger train [37] running on a rigid track with the same geometry as that of the finite element model. The vehicle analysis uses new UIC60 and S1002 profiles for the rails and wheels, respectively. Both the rigid track used in vehicle analysis and the finite element track model are free from irregularities.

The simulation results selected for the discussion are the evolution of wheel-rail forces along the track length and the displacement of the rails over time at selected track lengths. The rail displacements are analyzed at the 675.3 and 1055.7 m marks, depicted as black dots in Figure 9. These track lengths correspond to the middle of a straight section and the middle of a curved section, where a steady state of the vehicle dynamics is expected.

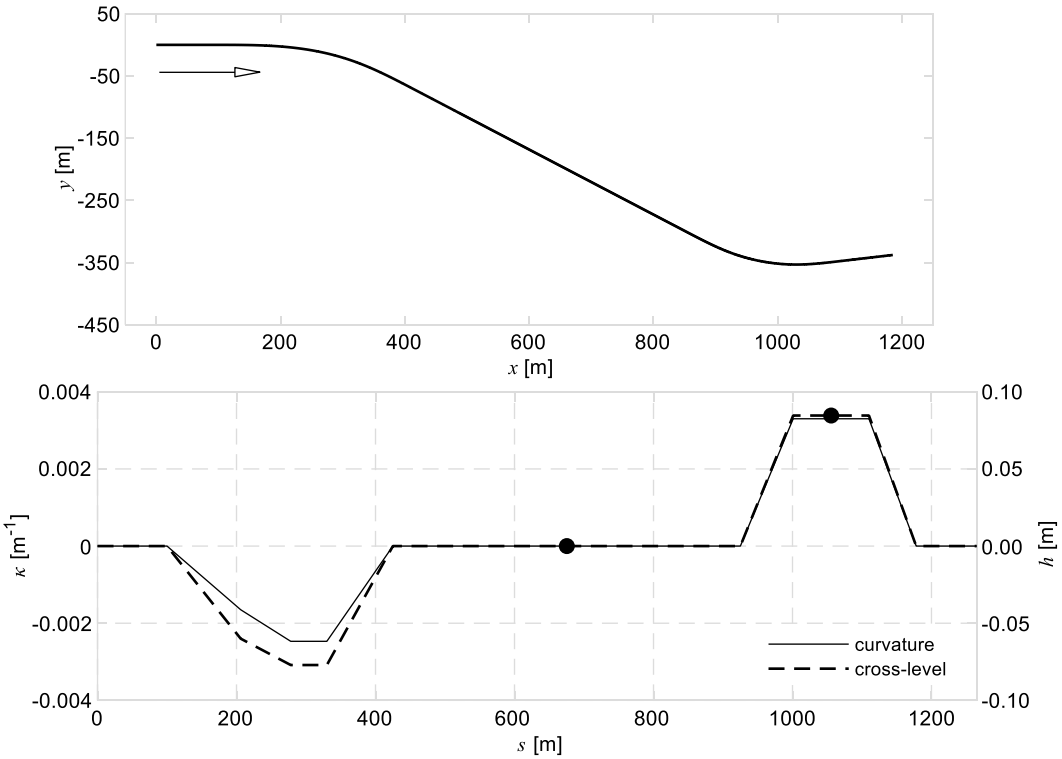

Figure 9: Top view, curvature, and cross-level of the railway track.

4.2 **Evolution of the wheel-rail forces**

In the following subsections, the vertical direction is defined by a vector with components $[0\ 0\ 1]^T$, while the lateral direction is defined by the cross product between the vertical direction and the rail tangent vector ξ_r. Figure 10 depicts the vertical and lateral net force on the rails obtained with the two alternative loading approaches. For both approaches, the net force on the rails shows a good agreement. The realistic forces exhibit peaks because the loading was extracted from a vehicle running on a perfectly rigid track. When the wheelset enters or exits a curve, there is a sudden interference in

the contact model without any damping from the rail, which increases the contact force for a few time steps. Despite showing that the net force of the two approaches is nearly identical, the comparison does not provide enough information on how the loads are transmitted to the track. The loads are transmitted from the wheelsets to the track via several contact points, with the forces at each point depending on the dynamic behavior of the vehicle. The simplified loading lacks this physical coherence that is inherent to the realistic loading approach.

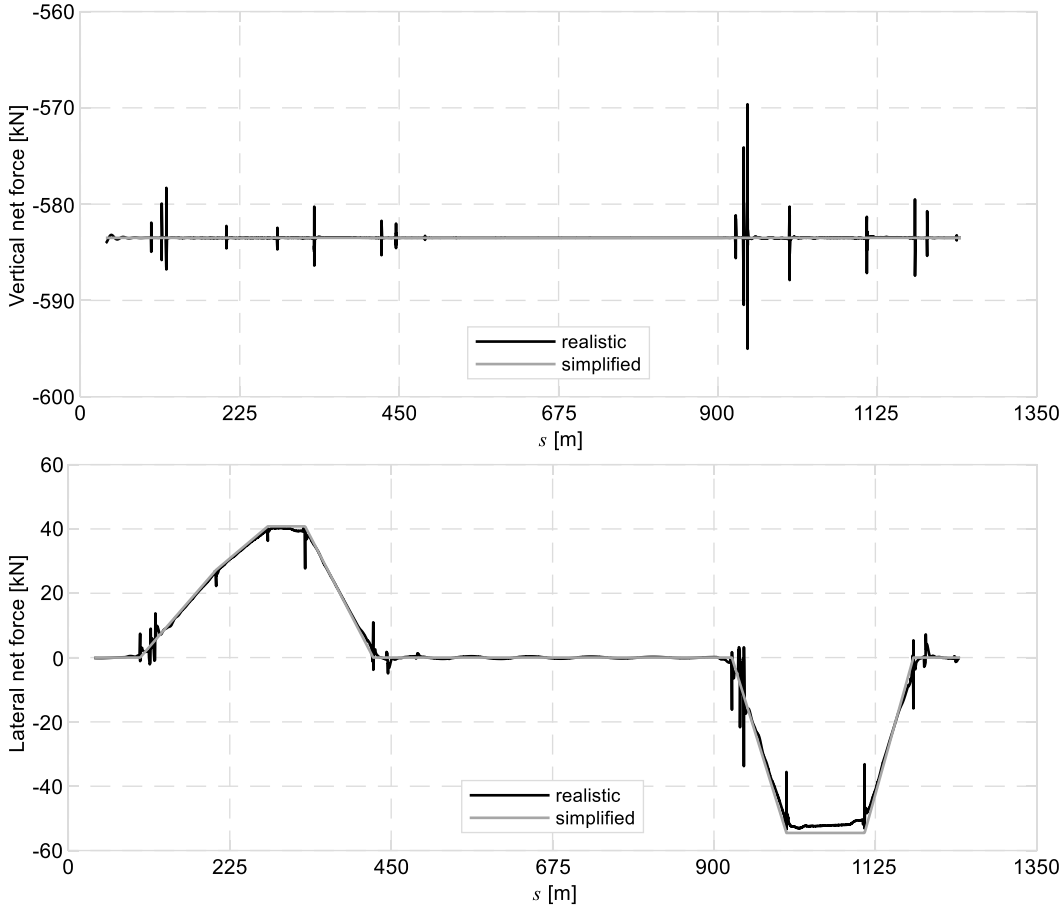

Figure 10: Vertical and lateral net force on the rails.

A passenger railway vehicle generally comprises two bogie frames, front and rear, with each bogie frame comprising two wheelsets, leading and trailing. Although the wheel-rail forces of the front and rear bogie are not the same, they present a similar evolution over the track length. Therefore, Figures 11 and 12 provide a comparison between the two loading approaches of the wheel-rail forces of the front bogie. The Figures only depict one wheel of the simplified loading approach because this method

prescribes the same load to every wheel. The realistic and simplified loading show a good agreement in both the vertical and lateral direction over the straight sections. Note that after the first curve, the vertical forces due to the realistic loading show a damped oscillation around those of the simplified loading.

On the other hand, there is no agreement between the loading approaches in either direction over the curved sections. In the vertical direction, the realistic loading captures the weight transfer that occurs to the outer rails, as observed in Figures 11 and 12, which is prevalent on the leading wheelset. On the lateral direction, contrary to the simplified loading, the forces applied on each wheel due to the realistic loading present different magnitudes. The realistic loading subjects the leading wheelset to higher loads than those in the trailing wheelsets, with the forces on each wheel presenting opposite directions. Furthermore, when compared to the simplified loading, the leading wheelset is subjected to higher loads, while the trailing wheelset is subjected to lower loads. The prediction of the wheel-rail loads provided by the two loading approaches is significantly different. The realistic loading shows that the assumption of equal distribution of the lateral net force over the rails is not accurate. Finally, considering the direction of the loads, the evolution of the simplified loading represents an underestimation of the realistic load on the outer wheel of a curved track section.

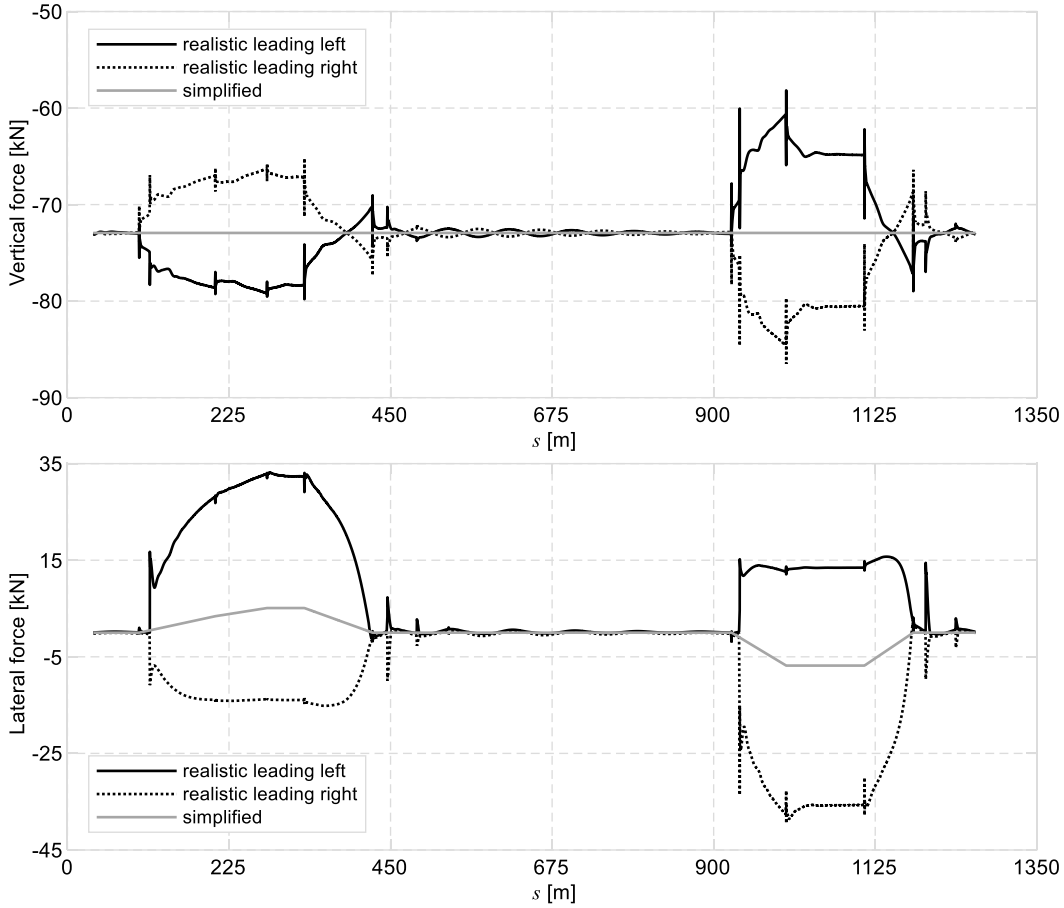

Figure 11: Wheel-rail forces of the front bogie leading wheelset.

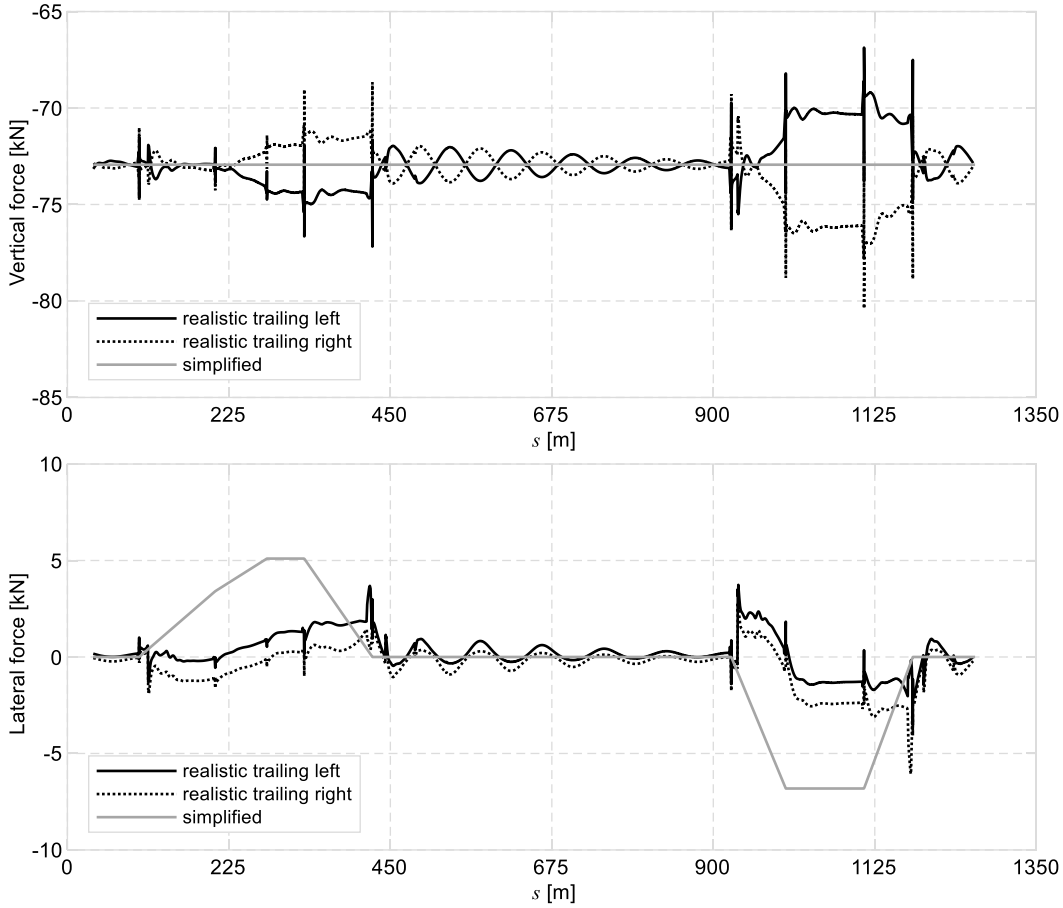

Figure 12: Wheel-rail forces of the front bogie trailing wheelset.

4.3 Rail displacement over time

The material properties used in this track model were collected from references which present different track models. Therefore, there is no guarantee that this model will behave as the models in the references, or a real track. Validation of the model is not addressed here and is left as a future development. Despite this, the analysis of the displacements of the rails still provides relevant information about the differences

between the two loading scenarios. Figure 13 (a) depicts the vertical and lateral displacement of the rail nodes at the 675.3 m mark, i.e., the second straight section. Both loading approaches produce virtually the same displacement in the vertical direction. Albeit with small deviations, the lateral displacements of the rails resulting from the two loading approaches present roughly the same shapes and magnitudes. In the realistic loading approach, the difference between the left and right rail lateral displacements is a result of the hunting oscillation, a self-adjusting motion of the wheelset. The assumption of a simplified loading seems reasonable for a vehicle running on a straight track with no irregularities and no flange contact.

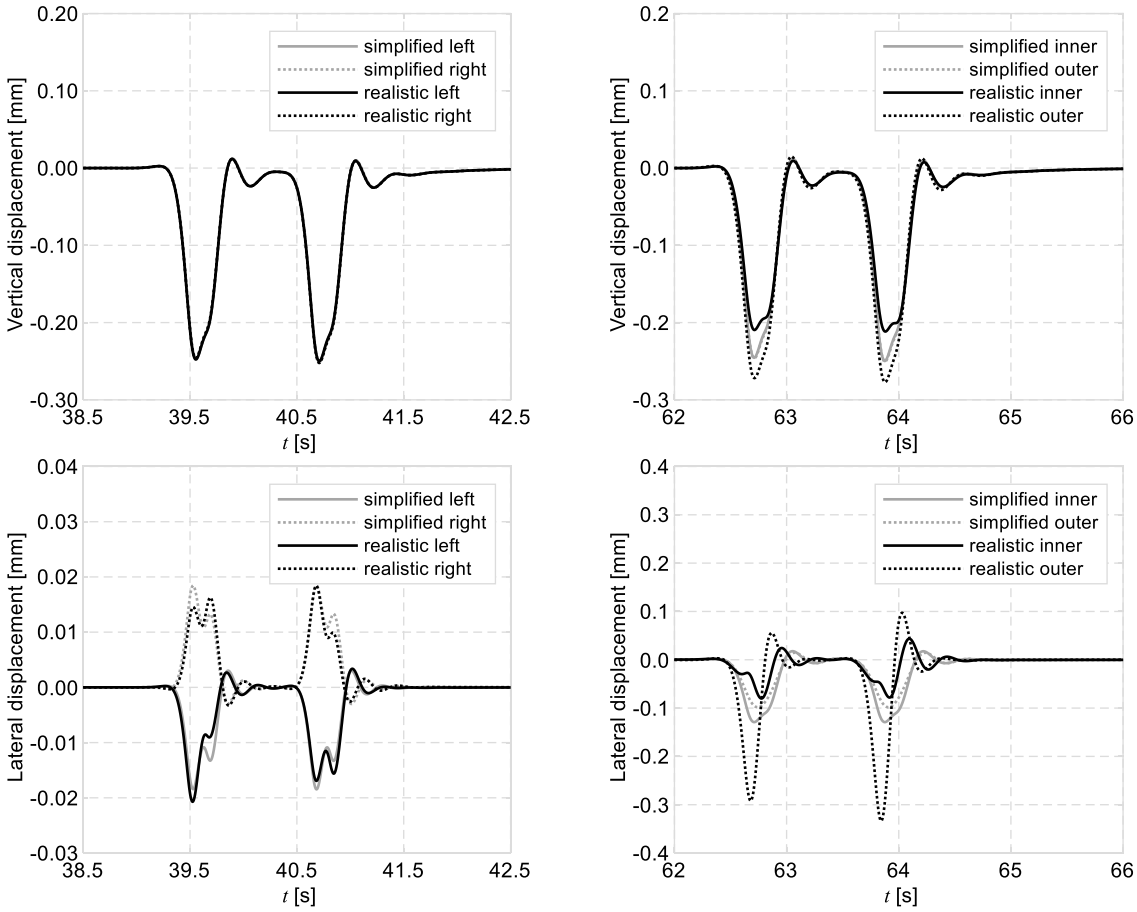

Figure 13: Displacement of the rail nodes: (a) on the straight section (s = 675.3 m), and (b) on the curved section (s = 1055.7 m).

Figure 13 (b) shows the vertical and lateral displacement of the rail nodes at the 1055.7 m mark, i.e., the second curved section. For convenience, the left and right rail are referred to as inner and outer rail with respect to the curve. For both loading approaches, the evolution of the vertical displacement is similar to that of the straight

section. In the simplified loading, the displacements of the left and right rail are virtually the same, while in the realistic loading, the displacements present some variations, with the outer rail presenting larger displacements due to the vehicle weight transfer. In the lateral direction, the displacements produced by the simplified loading present similar shapes but with a small difference in magnitude. On the other hand, in the realistic loading, the outer and inner rail behave differently, with the former being subjected to larger deformations. In this case, the simplified loading does not provide an accurate representation of the behavior of the track.

5 CONCLUSIONS

This work presents a methodology to automatically generate finite element meshes of railway tracks with arbitrary geometry. The methodology allows building tracks models given that track design geometry, irregularities, and material and geometric properties are provided. The track model presented in this work is used for the dynamic analyses of railway vehicles, which typically involve long track lengths. Therefore, the ballast or slab is modeled using spring-damper elements to ease the computational burden of the procedure. Although this modeling approach is insufficient for geotechnical studies, the presented methodology can be adapted by substituting the spring-damper elements by continuum elements. Accurate representation of track geometry and flexibility, together with suitable contact models, enables the studies to be performed over

curved track sections. A comparative study on the dynamics of a track is performed to highlight the difference between using prescribed and realistic loading over curved sections. However, note that the track and vehicle analyses are decoupled. Therefore, this study does not consider the flexibility of the rail in the evaluation of the wheel-rail contact forces. In future works, a co-simulation procedure where both the finite element and multibody codes run concurrently will be employed to capture the coupling between the vehicle and track dynamics [37,74,75]. However, by performing a dynamic analysis of a track using the wheel-rail force history extracted from a multibody analysis, in which the track is modeled as a rigid structure, lowers the computational burden of the procedure and still provides useful insights. The simplified loading, typically used in track dimensioning, is a reasonable approach for analyses on straight track sections. However, caution is advised when considering this approach on curved track sections. The results show that the lateral force provided by the simplified loading approach corresponds to an underestimation of the realistic contact force developed between the leading wheelset and the outer rail of the curve. Consequently, the prescribed and realistic loading approaches lead to different track behaviors, especially noticeable in the lateral direction.

ACKNOWLEDGEMENTS

The first author expresses his gratitude to the Portuguese Foundation for Science and Technology (*Fundação para a Ciência e a Tecnologia*) and the Luso-American

Development Foundation (*Fundação Luso-Americana para o Desenvolvimento*) through the grants PD/BD/128138/2016 and project – 140/2019, respectively. The third author expresses his gratitude to the Portuguese Foundation for Science and Technology through the PhD grant SFRH/BD/96695/2013. This work was supported by the Portuguese Foundation for Science and Technology, through IDMEC, under LAETA, project UIDB/50022/2020.

REFERENCES

1. Nikravesh PE. *Computer-Aided Analysis of Mechanical Systems*. Englewood Cliffs, New Jersey: Prentice-Hall, 1988.

2. Schiehlen W, Guse N, Seifried R. Multibody dynamics in computational mechanics and engineering applications. *Comput Methods Appl Mech Eng* 2006; 195: 5509–5522.

3. Magalhaes H, Madeira JFA, Ambrosio J, et al. Railway Vehicle Performance Optimization Using Virtual Homologation. *Veh Syst Dyn*. Epub ahead of print 2016. DOI: 10.1080/00423114.2016.1196821.

4. Polach O, Evans J. Simulations of Running Dynamics for Vehicle Acceptance: Application and Validation. *Int J Railw Technol* 2013; 2: 59–84.

5. Stichel S, Jönsson P-A, Casanueva C, et al. Modelling and Simulation of Freight

Wagon with Special attention to the Prediction of Track Damage. *Int J Railw Technol* 2014; 3: 1–36.

6. Bruni S, Vinolas J, Berg M, et al. Modelling of suspension components in a rail vehicle dynamics context. *Veh Syst Dyn* 2011; 49: 1021–1072.

7. Qazizadeh A, Persson R, Stichel S. Preparation and Execution of On-track Tests with Active Vertical Secondary Suspension. *Int J Railw Technol* 2015; 4: 29–46.

8. Kuka N, Ariaudo C, Verardi R. Modelling and Simulation of Tilting Vehicles. *Int J Railw Technol* 2013; 2: 63–82.

9. Marques F, Souto AP, Flores P. On the constraints violation in forward dynamics of multibody systems. *Multibody Syst Dyn* 2017; 39: 385–419.

10. Ambrósio J, Pombo J. A unified formulation for mechanical joints with and without clearances/bushings and/or stops in the framework of multibody systems. *Multibody Syst Dyn* 2018; 42: 317–345.

11. Tian Q, Flores P, Lankarani HM. A comprehensive survey of the analytical, numerical and experimental methodologies for dynamics of multibody mechanical systems with clearance or imperfect joints. *Mech Mach Theory* 2018; 122: 1–57.

12. Magalhães H, Ambrosio J, Pombo J, et al. Railway vehicle modelling for the vehicle-track interaction compatibility analysis. *Proc Inst Mech Eng Part K J Multi-body Dyn* 2016; 230: 251–267.

13. Goodall RM, Bruni S, Facchinetti A. Active Control in Railway Vehicles. *Int J Railw Technol* 2012; 1: 57–85.

14. Lorsch P, Algermissen S, Sinapius M. Concepts and Simulated Testing of Active Railway-Wheels. *Int J Railw Technol* 2013; 2: 65–78.

15. Kalker JJ. *Three-Dimensional Elastic Bodies in Rolling Contact*. Dordrecht, The Netherlands: Kluwer Academic Publishers, 1990. Epub ahead of print 1990. DOI: 10.1007/978-94-015-7889-9.

16. Polach O. A Fast Wheel-Rail Forces Calculation Computer Code. *Veh Syst Dyn* 1999; 33: 728–739.

17. Pombo J, Ambrósio J, Silva M. A New Wheel-Rail Contact Model for Railway Dynamics. *Veh Syst Dyn* 2007; 45: 165–189.

18. Pombo J, Ambrósio J. Application of a Wheel-Rail Contact Model to Railway Dynamics in Small Radius Curved Tracks. *Multibody Syst Dyn* 2008; 19: 91–114.

19. Magalhães H, Marques F, Liu B, et al. Implementation of a non-Hertzian contact model for railway dynamic application. *Multibody Syst Dyn* 2019; 1–38.

20. Haigermoser A, Luber B, Rauh J, et al. Road and track irregularities: measurement, assessment and simulation. *Veh Syst Dyn* 2015; 53: 878–957.

21. Pombo J, Ambrósio J. An Alternative Method to Include Track Irregularities in

Railway Vehicle Dynamic Analyses. *Nonlinear Dyn* 2012; 68: 161–176.

22. Popp K, Kruse H, Kaiser I. Vehicle-track dynamics in the mid-frequency range. *Veh Syst Dyn* 1999; 31: 423–464.

23. Di Gialleonardo E, Braghin F, Bruni S. The influence of track modelling options on the simulation of rail vehicle dynamics. *J Sound Vib* 2012; 331: 4246–4258.

24. Escalona JL, Sugiyama H, Shabana AA. Modelling of structural flexiblity in multibody railroad vehicle systems. *Veh Syst Dyn* 2013; 51: 1027–1058.

25. Pombo J, Ambrósio J, Silva M. A new wheel–rail contact model for railway dynamics. *Veh Syst Dyn* 2007; 45: 165–189.

26. Chaar N, Berg M. Simulation of vehicle-track interaction with flexible wheelsets, moving track models and field tests. *Veh Syst Dyn* 2006; 44: 921–931.

27. Nakajima T, Feldmeier C, Sugiyama H. Flexible moving track model for curve negotiation analysis of railroad vehicles with rail roll deflection. *Proc Inst Mech Eng Part K J Multi-body Dyn* 2016; 230: 85–98.

28. Zhai WM, Cai CB, Guo SZ. Coupling Model of Vertical and Lateral Vehicle/Track Interactions. *Veh Syst Dyn* 1996; 26: 61–79.

29. Zhai WM, Wang KY. Lateral interactions of trains and tracks on small-radius curves: simulation and experiment. *Veh Syst Dyn* 2006; 44: 520–530.

30. Zhai W, Wang K. Lateral hunting stability of railway vehicles running on elastic track structures. *J Comput Nonlinear Dyn* 2010; 5: 1–9.

31. Shabana AA, Chamorro R, Rathod C. A multi-body system approach for finite-element modelling of rail flexibility in railroad vehicle applications. *Proc Inst Mech Eng Part K J Multi-body Dyn* 2008; 222: 1–15.

32. Shabana AA, Sanborn G. An Alternative Simple Multibody System Approach for Modelling Rail Flexibility in Railroad Vehicle Dynamics. *Inst Mech Eng Part K J Multi-body Dyn* 2009; 223: 107--120.

33. Rathod C, Chamorro R, Escalona JL, et al. Validation of three-dimensional multi-body system approach for modelling track flexibility. *Proc Inst Mech Eng Part K J Multi-body Dyn* 2009; 223: 269–282.

34. Torstensson PT, Pieringer A, Nielsen JCO. Simulation of rail roughness growth on small radius curves using a non-Hertzian and non-steady wheel–rail contact model. *Wear* 2014; 314: 241–253.

35. Kaiser I. Refining the modelling of vehicle–track interaction. *Veh Syst Dyn* 2012; 50: 229–243.

36. Martínez-Casas J, Di Gialleonardo E, Bruni S, et al. A comprehensive model of the railway wheelset-track interaction in curves. *J Sound Vib* 2014; 333: 4152–4169.

37. Antunes P, Magalhães H, Ambrósio J, et al. A co-simulation approach to the wheel–rail contact with flexible railway track. *Multibody Syst Dyn* 2019; 45: 245–272.

38. Varandas JN, Paixão A, Fortunato E. A study on the dynamic train-track interaction over cut-fill transitions on buried culverts. *Comput Struct* 2017; 189: 49–61.

39. Francisco A, Paixão A, Varandas JN, et al. Short soil–binder columns in railway track reinforcement: three–dimensional numerical studies considering the train–track interaction. *Comput Geotech* 2018; 98: 8–16.

40. Wang H, Markine VL. Methodology for the comprehensive analysis of railway transition zones. *Comput Geotech* 2018; 99: 64–79.

41. Wang H, Markine V. Corrective countermeasure for track transition zones in railways: Adjustable fastener. *Eng Struct* 2018; 169: 1–14.

42. Blanco-Saura AE, Velarte-González JL, Ribes-Llario F, et al. Study of the dynamic vehicle-track interaction in a railway turnout. *Multibody Syst Dyn* 2018; 43: 21–36.

43. Paixão A, Varandas JN, Fortunato E, et al. Numerical simulations to improve the use of under sleeper pads at transition zones to railway bridges. *Eng Struct* 2018; 164: 169–182.

44. Sainz-Aja J, Pombo J, Tholken D, et al. Dynamic calibration of slab track models for railway applications using full-scale testing. *Comput Struct*; 228. Epub ahead of print 1 February 2020. DOI: 10.1016/j.compstruc.2019.106180.

45. Mezher SB, Connolly DP, Woodward PK, et al. Railway critical velocity - Analytical prediction and analysis. *Transp Geotech* 2016; 6: 84–96.

46. Varandas JN, Paixão A, Fortunato E, et al. Numerical Modelling of Railway Bridge Approaches: Influence of Soil Non-Linearity. *Int J Railw Technol* 2014; 3: 73–95.

47. Zhu Z, Gong W, Wang L, et al. An efficient multi-time-step method for train-track-bridge interaction. *Comput Struct* 2018; 196: 36–48.

48. Chen Z, Zhai W, Yin Q. Analysis of structural stresses of tracks and vehicle dynamic responses in train–track–bridge system with pier settlement. *Proc Inst Mech Eng Part F J Rail Rapid Transit* 2018; 232: 421–434.

49. CEN. EN 1991-2 Eurocode 1: Actions on structures - Part 2: Traffic loads on bridges.

50. Iwnicki S, Bevan AJ. Damage to Railway Wheels and Rails: A Review of the Causes, Prediction Methods, Reduction and Allocation of Costs. *Int J Railw Technol* 2012; 1: 121–146.

51. Kuka N, Verardi R, Ariaudo C, et al. Impact of maintenance conditions of vehicle

components on the vehicle–track interaction loads. *Proc Inst Mech Eng Part C J Mech Eng Sci* 2018; 232: 2626–2641.

52. Sugiyama H, Yada M, H. Y, et al. Wheel and Rail Profile Wear on Small Radius Curved Tracks and its Effect on Derailment Coefficients: Measurement and Simulation. *Int J Railw Technol* 2013; 2: 85--98 (DOI:10.4203/ijrt.2.4.5).

53. Sañudo R, Markine V, Pombo J. Study on Different Solutions to Reduce the Dynamic Impacts in Transition Zones for High-Speed Rail. *J Theor Appl Vib Acoust* 2017; 3: 199–222.

54. Pombo J. Application of a Computational Tool to Study the Influence of Worn Wheels on Railway Vehicle Dynamics. *J Softw Eng Appl* 2012; 05: 51--61.

55. Dukkipati R V, Amyot JR. *Computer-Aided Simulation in Railway Dynamics*. New York, New York: M. Dekker Inc., 1988.

56. Garg VK, Dukkipati R V. *Dynamics of Railway Vehicle Systems*. New York, New York: Academic Press, 1984.

57. Ambrósio J, Antunes P, Pombo J. On the requirements of interpolating polynomials for path motion constraints. In: Kecskeméthy A, Geu Flores F (eds) *Mechanisms and Machine Science*. Springer International Publishing, 2015, pp. 179–197.

58. Pombo J, Ambrósio JAC. General Spatial Curve Joint for Rail Guided Vehicles:

Kinematics and Dynamics. *Multibody Syst Dyn* 2003; 9: 237–264.

59. Bathe K-J. *Finite element procedures*. Englewood Cliffs, N.J.: Prentice Hall, 1996.

60. Zienkiewicz O, Taylor R. *The Finite Element Method*. Woburn, Massachussetts: Butterwort-Heinemann, 2000.

61. Recuero AM, Escalona JL, Shabana AA. Finite-element analysis of unsupported sleepers using three-dimensional wheel-rail contact formulation. *Proc Inst Mech Eng Part K J Multi-body Dyn* 2011; 225: 153–165.

62. Li D, Selig ET. Method for Railroad Track Foundation Design. I: Development. *J Geotech Geoenvironmental Eng* 1998; 124: 316–322.

63. SMARTRACK Project - System Dynamics Assessment of Railway Tracks: A Vehicle-Infrastructure Integrated Approach FCT PTDC/EME-PME/101419/2008. 2013.

64. CEN. EN 13674-1 Railway applications - Track - Rail - Part 1: Vignole railway rails 46 kg/m and above.

65. Zhai W, Wang K, Cai C. Fundamentals of vehicle–track coupled dynamics. *Veh Syst Dyn* 2009; 47: 1349–1376.

66. Kassa E, Andersson C, Nielsen JCO. Simulation of dynamic interaction between train and railway turnout. *Veh Syst Dyn* 2006; 44: 247–258.

67. Zhai WM, Wang KY, Lin JH. Modelling and experiment of railway ballast vibrations. *J Sound Vib* 2004; 270: 673–683.

68. Esveld C. Improved knowledge of CWR track. *Interact Conf cost Eff Saf Asp Railw track*.

69. Przemieniecki JS. *Theory of Matrix Structural Analysis*. New York: McGraw-Hill, 1968.

70. CEN. EN 13803-1 Railway applications — Track — Track alignment design parameters — Track gauges 1435 mm and wider Part 1: Plain line.

71. Lankarani HM, Nikravesh PE. A Contact Force Model with Hysteresis Damping for Impact Analysis of Multibody Systems. *AMSE J Mech Des* 1990; 112: 369–376.

72. Lankarani HM, Nikravesh PE. Continuous Contact Force Models for Impact Analysis in Multibody Systems. *Nonlinear Dyn* 1994; 5: 193–207.

73. Hughes T. *The Finite Element Method: Linear Static and Dynamic Finite Element Analysis*. Englewood Cliffs, New Jersey: Prentice-Hall, 1987.

74. El-Ghandour AI, Hamper MB, Foster CD. Coupled finite element and multibody system dynamics modeling of a three-dimensional railroad system. *Proc Inst Mech Eng Part F J Rail Rapid Transit* 2016; 230: 283–294.

75. El-Ghandour AI, Foster CD. Coupled finite element and multibody systems dynamics modelling for the investigation of the bridge approach problem. *Proc Inst Mech Eng Part F J Rail Rapid Transit* 2019; 095440971982859.